THE JOURNAL OF PHYSICAL CHEMISTRY C
A JOURNAL OF THE AMERICAN CHEMICAL SOCIETY

pubs.acs.org/JPCC

Article

Influence of Peripheral and Ancillary Changes on the Electron Transport of $^{HS}3d^5$ Fe^{III} Metallosurfactants – Substituents, Chain Length, Subphase Polarity, and Junction Electrodes

Gibson Kirui, Widana Kaushalya, S. Sameera Perera, Alice R. Walker, and Cláudio N. Verani*

Cite This: https://doi.org/10.1021/acs.jpcc.4c02249

Read Online

ACCESS | Metrics & More | Article Recommendations | Supporting Information

ABSTRACT: Our ongoing efforts to design metallosurfactants capable of directional electron transport led to pondering on the effects of peripheral changes, and the development of $3d^5$ Fe^{III} systems where iodo groups replace the usual *tert*-butyl groups attached to phenylenediamine-bridged phenolate donors. We present the results for two newly designed metallosurfactants, namely, $[Fe^{III}(L^1)Cl]$ (**1**) and $[Fe^{III}(L^2)Cl]$ (**2**), where **1** incorporates shorter hydrophilic alkoxy chains than **2**. These species had their electronic and electrochemical properties evaluated by experimental and computational methods. We also considered ancillary changes, such as subphase polarity effects on their interfacial properties of Pockels-Langmuir monolayer films on water and Langmuir–Blodgett monolayer films on gold electrodes, evaluated by multiple surface-dedicated methods and probed for directional electron transfer in Au|LB|Au and Au|LB|EGaIn junctions, prior to comparison to the previously published *t*-Bu-substituted standard $[Fe^{III}(L^{tBu})Cl]$ (**3**). These modifications led to significant modulation of metal-based SOMO energy levels toward the Fermi energy levels of the electrode from 1.0 eV in **3** to ca. 0.5 eV in **1** and **2**, which result in better rectification ratios (RR = [I at − V/I at + V]) than those for **3**.

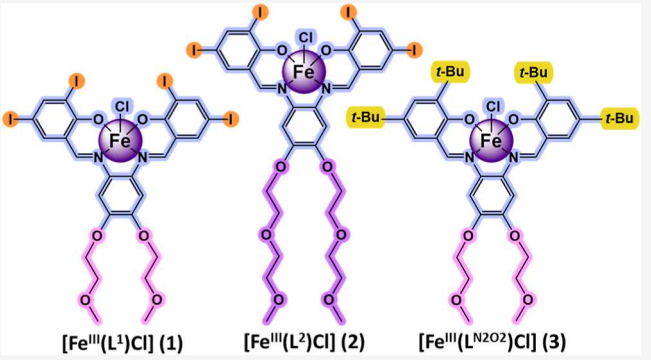

INTRODUCTION

Directional electron transport through a molecular monolayer placed between two electrodes—or an $E_1|monolayer|E_2$ molecular junction— emulates the properties of a solid state diode in electronic circuits and may become relevant to the development of circuitry to next-generation quantum systems.[1−5] Classic unimolecular transport[6,7] requires explicit donor and acceptor moieties engaging in electron transport from one electrode to the LUMO of the acceptor, while another electron is transferred simultaneously from the HOMO of the donor to the next electrode. After formation of this $[D^+A^-]$ excited state, the electron in A^{LUMO} relaxes to D^{HOMO}, replenishing the [DA] state.

$$E_1|DA|E_2 \rightarrow E_1^-|D^+A^-|E_2^+ \rightarrow E_1^-|DA|E_2^+ \quad (1)$$

The main factor enabling electron transport is the matching between the electrode Fermi level, usually Au at −5.1 eV, and the energy of the tunneling molecular orbital. Focusing on 3d metal coordination compounds, we have observed a new form of directional transport in a high-spin $3d^5$ iron(III) metallosurfactant $[Fe^{III}(L^{N2O3})]$, exhibiting a trigonal bipyramidal e"($3d_{xz}^1$, $3d_{yz}^1$) e'($3d_{x2\text{-}y2}^1$, $3d_{xy}^1$) $a_1'(3d_{z2}^1)$ environment.[8−11] Instead of the expected involvement of *highest occupied* HOMO[12,13] or *lowest unoccupied* LUMO,[14,15] this species mediates electron transport through the lowest lying *singly occupied* SOMOs described as the linear combination of $3d_{xz}+3d_{yz}$ orbitals and found within 1 eV from the electrode Fermi level. This unusual Fermi-SOMO transport prompted us to examine several $3d^n$ electronic configurations, and how the energies of LUMO, SOMO, and HOMO orbitals are tuned by the number of electrons to match the Fermi levels and enable directional transport. To date we have examined Au|LB|Au junctions containing Langmuir–Blodgett films of $3d^1$, $3d^3$, $^{HS}3d^4$ $^{HS}3d^5$, and $3d^9$ metallosurfactants containing $[N_2O_2]$ or $[N_2O_3]$ ligands.[16−20] Interestingly, the $3d^1$ $[V = O^{IV}(L^{N2O2})]$, $^{HS}3d^4$ $[Mn^{III}(L^{N2O2})(s)_2]Cl$, $^{HS}3d^5$ $[Fe^{III}(L^{N2O2})Cl]$, and $[Fe^{III}(L^{N2O3})]$ engage in directional electron transfer through the metal SOMO via different mechanisms; while the $V = O^{IV}$ species relies on the $3d_{xy}$-based MO about 0.5 eV *below* the Fermi level, the Mn^{III} species relies on a well-defined $3d_{yz}$ MO rather than the $(3d_{xz}+3d_{yz})$ linear combination observed for Fe^{III} species, both within ∼1 eV *above* the Fermi levels. The

Received: April 5, 2024
Revised: May 20, 2024
Accepted: June 7, 2024

$3d^3$ $[Cr^{III}(L^{N2O2})(s)_2]Cl$ shows energy mismatched SOMOs and requires transport through a *ligand-based* HOMO about 0.8 eV *below* Fermi. Finally, the $3d^9$ $[Cu^{II}(L^{N2O2})]$ only leaves the highest $3d_{x2-y2}$ for transport and acts as an insulator.

In this study, we expand our inquiry from electronic configurations to the influence of peripheral molecular changes, such as the role of substituents and chain lengths, as well as ancillary effects such as subphase polarity and electrode material. We develop two new metallosurfactants, namely, $[Fe^{III}(L^1)Cl]$ (**1**) with regular length methoxyethoxy ($H_3C{-}O(CH_2)_2{-}O{-}$) chains, and $[Fe^{III}(L^2)Cl]$ (**2**) with longer methoxy-diethoxy ($H_3C{-}(O{-}CH_2)_2{-}O{-}$) chains in the 4,5-positions of the phenylenediamine ring in which the common apolar and electron-donating *t*-Butyl substituents of the phenolate rings found in our previous $[Fe^{III}(L^{N2O2})Cl]$—here renamed as $[Fe^{III}(L^{tBu})Cl]$ (**3**)—are replaced by polar and electron-withdrawing iodo substituents (Figure 1). The

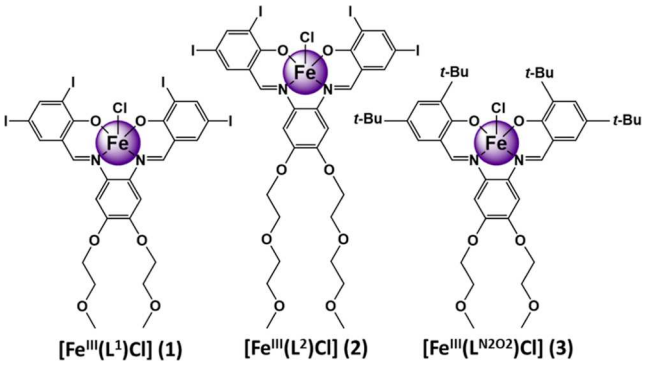

Figure 1. $3d^5$ Fe^{III}-containing metallosurfactants **1**−**3**.

electronic properties of species **1** and **2** are examined by a suite of spectroscopic, electrochemical, and DFT methods, their Pockels-Langmuir (PL) film compression and Langmuir−Blodgett film deposition are investigated under regular (water), hyper-polar (0.1 M NaCl), and hypo-polar (1% isopropanol) air|liquid interfaces, the characteristics of the resulting air|solid films are evaluated by IR-reflection absorption, scanning electron microscopy (SEM), and X-ray photoelectron spectroscopy (XPS), and their electron transport response is assessed by current/potential (I−V) curves on Au|LB|Au and EGaIn|LB|Au junctions, with Fermi/MO energies being assessed by electrochemical conversion and UV photoelectron spectroscopy. The results are given as follows.

■ EXPERIMENTAL SECTION

Materials and Methods. Reagents and solvents were used as purchased from commercial sources. A Varian 600 MHz instrument was used for ^1H NMR spectra using $CDCl_3$ as the solvent. Chemical shifts (δ) are reported in ppm. The Fourier-transform infrared (FTIR) spectrum of ligands and the complexes were recorded as KBr pellets using either a Bruker Tensor 27 or an INVENIO spectrometer in the range of 4000−400 cm^{-1} using 64 scans. A Shimadzu UV-3600 UV−vis−NIR spectrophotometer was used to measure the electronic spectra from 200−1100 cm^{-1}. Elemental analyses of complexes were performed by Midwest Microlab, Indianapolis, Indiana USA, using V_2O_5 for complete combustion. High-resolution ESI mass spectrometry data were acquired using a Thermo LTQ-Orbitrap XL spectrometer and Micromass LCT Premier XE (TOF) mass spectrometer.

Syntheses. *Ligand (((4,5-bis(2-Methoxyethoxy)-1,2-Phenylene)bis(Azaneylylidene)bis(Me-Thaneylyli- Dene))bis-(2,4-Diiodophenol), H_2L^1.* A solution of 3,5-di-iodo-2-hydroxybenzaldehyde (3.80 g, 10.30 mmol) in dry methanol (30 mL) was added into a solution of 4,5-bis(2-methoxyethoxy)-benzene-1,2-diamine (1.20 g, 4.70 mmol) in anhydrous methanol (15 mL). The mixture was heated at reflux for 1 h under inert conditions. The resulting orange turbid solution was stored at 4 °C overnight yielding a precipitate, which was filtered, washed with small amounts of cold methanol, and dried under vacuum to attain an orange microcrystalline powder. Yield: 82%. High res. ESI (m/z+) in CH_2Cl_2/MeOH = 968.7844 for $[C_{26}H_{24}I_4N_2O_6 + H^+]$ (calculated = 968.7888), in agreement with −4.078 ppm difference. ^1H NMR, ppm ($CDCl_3$, 600 MHz): 3.47 (s, 6H), 3.79 (t, 4H), 4.22 (t, 4H), 6.86 (s, $2H_{ph}$), 7.64 (d, $2H_{ph}$), 8.08 (d, $2H_{ph}$), 8.39 (s, 2H). Melting point: 210 °C. IR (KBr, cm^{-1}) 3444 (νO−H), 2817−3055 (νC−H), 1508 (νC = C, aromatic), 1434 (νC = C, aromatic), 1607 (νC = N), 1267 (νC−O−C), 1156(νC−O−C).

Ligand (((4,5-bis(2-Methoxyethoxy)Ethoxy)-1,2-Phenylene)bis(Azaneylylidene)bis(Metha-Neylylidene))bis-(2,4-Diiodophenol), H_2L^2. The ligand was obtained in a similar way as described above by adding 3,5-di-iodo-2-hydroxybenzaldehyde (3.40 g, 9.10 mmol) to 4,5-bis(2-(2-methoxyethoxy)ethoxy)benzene-1,2-diamine (1.25 g, 3.70 mmol). Dark orange microcrystalline powder. Yield: 94%. High res. ESI (m/z+) in CH_2Cl_2/MeOH = 1056.8397 for $[C_{30}H_{32}I_4N_2O_8 + H^+]$ (calculated = 1056.8410), in agreement with −1.2176 ppm difference. ^1H NMR, ppm ($CDCl_3$, 600 MHz): 3.37 (s, 6H), 3.57 (t, 4H), 3.72 (t, 4H), 3.89 (t, 4H), 4.24 (t, 4H), 6.89 (s, $2H_{ph}$), 7.65 (d, $2H_{ph}$), 8.08 (d, $2H_{ph}$), 8.41 (s, 2H). Melting point: 130 °C. IR (KBr, cm^{-1}) 2824−3054 (νC−H), 1509 (νC = C, aromatic), 1431 (νC = C, aromatic), 1606 (νC = N), 1267 (νC−O−C), 1157(νC−O−C).

Metallosurfactant $[Fe^{III}(L^1)Cl]$ (1). A mixture of $\mathbf{H_2L^1}$ (0.25 g, 0.26 mmol) and anhydrous $NaOCH_3$ (0.028 g, 0.52 mmol) in 15:5 mL of methanol: dichloromethane was treated with 5 mL of a methanolic solution of $FeCl_3.6H_2O$ (0.07 g, 0.26 mmol). The resulting solution was heated at 50 °C for 4 h. The reaction mixture was cooled to ambient temperature and stirred for 1 h. The solution was then filtered to attain a dark brown microcrystalline powder. Yield: 79%. High res. ESI (m/z+) in CH_3OH = 1021.7024 (100%) for $[C_{26}H_{22}N_2I_4O_6Fe]^+$ (calculated = 1021.7001), in agreement with 2.3418 ppm difference. Melting point: >300 °C Anal. Calc. for $[C_{26}H_{22}N_2I_4O_6FeCl]$: C, 29.53; H, 2.10; N, 2.65%. Found: C, 29.90; H, 1.95; N, 2.73%. IR (KBr, cm^{-1}) 2820−3046 (νC−H), 1600 (νC = C, aromatic), 1496 (νC = C, aromatic) 1575 (νC = N), 1363 (νC−O−C), 1273 (νC−O−C).

Metallosurfactant $[Fe^{III}(L^2)Cl]$ (2). This species was obtained in a similar way as described above by adding $\mathbf{H_2L^2}$ (0.50 g, 0.47 mmol), $NaOCH_3$ (0.05 g, 0.95 mmol), and $FeCl_3.6H_2O$ (0.13 g, 0.47 mmol). Dark brown microcrystalline powder. Yield: 80%. High res. ESI (m/z+) in CH_3OH = 1145.7282 (100%) for $[C_{30}H_{30}N_2I_4O_8FeCl + H^+]$ (calculated = 1145.7292), in agreement with −0.8382 ppm difference. Melting point: 251 °C. Anal. Calc. for $[C_{30}H_{30}N_2I_4O_8FeCl]$: C, 31.46; H, 2.64; N, 2.45%. Found: C, 31.32; H, 2.72; N, 2.50%. IR(KBr, cm^{-1}) 2824−2923 (νC−H), 1602 (νC = C, aromatic), 1496 (νC = C, aromatic) 1577 (νC = N), 1368 (νC−O−C), 1272 (νC−O−C).

https://doi.org/10.1021/acs.jpcc.4c02249
J. Phys. Chem. C XXXX, XXX, XXX−XXX

Electrochemistry. The electrochemical experiments were carried out at room temperature in an inert atmosphere using a BAS 50W voltammetric analyzer. A standard three-electrode cell was used with glassy carbon as the working electrode, Ag/AgCl as a reference electrode, and Pt wire as the auxiliary electrode. Cyclic voltammograms were recorded at 25 mV/s in dichloromethane and 19:1 dichloromethane: dimethyl sulfoxide solutions for species **1** and **2**, respectively, using tetrabutylammonium hexafluorophosphate ($TBAPF_6$) as the supporting electrolyte and ferrocene as the internal standard. All the potentials were therefore referenced vs. the potential of ferrocene.

Formation of Pockels–Langmuir and Langmuir–Blodgett Monolayer Films. To obtain the surface pressure against the average molecular area isotherms at the air/water interphase, an automated KSV Minitrough was used. Ultrapure water with a resistivity value of 18.0–18.1 MΩ/cm was obtained from a Barnstead NANOpure system and used as the subphase for all the experiments at 23 ± 0.3 °C temperature. Prior to each isothermal compression experiment, the vacuum was used to remove any impurities present at the surface of the aqueous subphase. The complexes were dissolved in spectra-grade volatile dichloromethane to prepare the spreading solutions with a concentration of 1 mg mL^{-1}. For each trial, approximately 25 to 30 μL of spreading solutions of complexes **1** and **2** was introduced over the subphase, and about 20 min of equilibration time was allowed before monolayer compressions. During each measurement, the paper Wilhelmy plates (20 × 10 mm) were used to measure the surface pressures at a barrier compression rate of 10 mm min^{-1}. At least three reproducible independent measurements were recorded for each complex.

Brewster Angle Microscopy. The Brewster angle microscopy (BAM) micrographs of metallosurfactants **1** and **2** were recorded using a CCD detector of KSV-Optrel BAM 300 with a HeNe laser (10 mW, 632.8 nm). A compression rate of 10 mm/min was chosen to maintain a homogeneous film growth on the monolayer. The field view of the microscope at 800 × 600 μm and the lateral resolution of about 2–4 μm was used.

Scanning Electron Microscopy. Monolayer morphology and thickness measurements were taken using a JSM-7600 FE field emission scanning electron microscope. One monolayer at different surface pressures was deposited on glass substrates for surface morphology analysis while 15 and 17 monolayers of **1** and **2**, respectively, were deposited on silicon thermal oxide wafers for cross-section thickness measurements. Each sample was loaded into the entry chamber at a desired pressure level and transferred to the analysis chamber while being held under vacuum (ca. 9.5 × 10^{-4} mbar) throughout the experiment. The surface morphology measurements of LB films were obtained under the low magnification (LM) mode under a magnification of 40×. On the other hand, cross-section images were captured and measured under the SEM mode under a magnification of 200,000 and 130,000× for metallosurfactants **1** and **2**, respectively. Every measurement was recorded at least three times, and the mean cross-section thickness was divided by the total number of layers for monolayer thickness approximation.

X-ray Photoelectron Spectroscopy. The Fe^{III} metallosurfactants in bulk and films were analyzed using the ThermoScientific Nexsa X-ray photoelectron spectrometer (XPS) with a hemispherical analyzer and monochromatic Al Kα (1486.7 eV) source. The powdered samples were mounted to a standard sample holder using conductive copper tape and the LB films using copper-spring clips. The sample holder was loaded into the entry-lock chamber and held under vacuum for about half an hour. After reaching the recommended vacuum level (4 × 10^{-7} mbar), the sample was transferred to the analysis chamber and kept at a pressure of around 1.8 × 10^{-7} mbar throughout the experiment. The high-resolution spectra were collected using 50 eV pass-energy, 0.1 eV energy step size, and 100 ms/step dwell time. Recorded spectra were analyzed using ThermoAvantage v5.9922 software to extract qualitative information. The C 1s, Fe 2p, and I 3d peaks were fitted using Voight functions.

Ultraviolet Photoelectron Spectroscopy. The LB film samples were characterized using the ThermoScientific Nexsa XPS equipped with ultraviolet photoelectron spectroscopy (UPS) capabilities. UPS experiments were performed with He I (21.20 eV) photon lines from a He-discharge lamp. LB film samples were mounted on a UPS bias sample holder using copper-spring clips. The samples from the entry-lock chamber, which was at a pressure of around 4 × 10^{-7} mbar were transferred to the analysis chamber. The vacuum level inside the analysis chamber was maintained at ∼3.6 × 10^{-7} mbar throughout the data acquisition time. A bias voltage of −10 V was applied to overcome the work function difference between the sample and the spectrometer. High-resolution UPS spectra were recorded using 2.00 eV pass-energy, 0.05 eV energy step size, and 150 ms/step dwell time. The recorded spectra were analyzed using ThermoAvantage v5.9922 software.

Assembly of Au|LB|Au and Au|LB|EGaIn Junctions and Measurement of I–V Curves. The Langmuir–Blodgett monolayers of metallosurfactants **1** and **2** were deposited on precleaned Ted Pella or SPI supplied gold-coated mica substrates at respective surface pressures of 24 and 25 mN m^{-1}. These films were dried in a desiccator for 5 days under reduced pressure. For Au|LB|Au junctions, the top gold electrode was deposited using shadow masking[6] with an Effa-Coater gold sputter yielding an assembly with 16 junctions. For Au|LB|EGaIn junctions, the top soft contact containing EGaIn material was made using the commercially available gallium indium eutectic under ambient conditions. The current–voltage (I–V) characteristics of the devices were measured using a Keithley 4200 semiconductor parameter analyzer coupled to a Signatone S-1160 Probe Station under ambient conditions. A total of 48 and 64 Au|LB|Au junctions were, respectively, analyzed for metallosurfactants **1** and **2**. Additionally, a total of 27 Au|LB|EGaIn junctions were analyzed for metallosurfactant **2.**

DFT Calculations. Symmetry unconstrained ground-state geometry optimizations were performed on each complex using spin unrestricted DFT[21] with Gaussian16, Rev.B.01.[22] The B3LYP functional was used[23,24] with a SDD basis set on the iron and a LANL2DZ basis set on the iodine atoms with their respective pseudopotentials. The 6-31G(d,p)[25,26] basis set was used on all the other atoms. Solvation effects in dichloromethane were accounted for with the implicit polarizable *continuum model (PCM),*[27,28] with ε = 8.93. Optimized structures were confirmed as minima by performing frequency calculations and verifying that there were no negative frequencies. Iso-density plots of orbitals were visualized using Gauss View 5.0.9,[29] with an isovalue of 0.05.

Vertical excitation energies and oscillator strengths for excited states S_1 to S_{150} were calculated using the GPU-accelerated TDDFT in TeraChem.[30,31] The calculations were

https://doi.org/10.1021/acs.jpcc.4c02249
J. Phys. Chem. C XXXX, XXX, XXX–XXX

performed using the B3LYP functional with LANL2DZ and pseudopotentials on both iron and iodine atoms and 6-31G(d,p) on all other atoms. The orbital transition of each excited state was characterized and visualized using Gauss View 5.0.9. Born−Oppenheimer molecular dynamics simulations were run for both iron complexes at the same level of theory for 1 ps in the *NPT* ensemble, including the PCM model (ε = 8.93) and with a 1 fs time step. The thermostat temperature was set to 300 K, with a Langevin thermo/barostat and a friction constant δ = 5 ps^{-1}.

RESULTS AND DISCUSSION

Rationale. Attaining directional electron transport requires good compatibility between electronic, redox, and film formation properties merged into a single metallosurfactant. We hypothesize that the introduction of electron-withdrawing iodo-substituents on the phenolate rings of the ligand framework will reduce electronic density around the metal center, leading to more accessible redox states. This will ensure the decrease and modulation of the energy associated with the frontier molecular orbital with respect to the Fermi energy level of the electrodes in E_1|monolayer|E_2 molecular junctions and facilitate electron transport. However, any change in substituents may lead to imbalance in the amphiphilic properties needed for film deposition. We further hypothesize that in order to retain good amphiphilic response, the length of the alkoxy chains or the subphase polarity during film deposition may require changes.

Synthesis and Characterization. The new salophen-based ligands H_2L^1 and H_2L^2, respectively, containing methoxyethoxy ($H_3C{-}O(CH_2)_2{-}O{-}$) and longer methoxy-diethoxy (H_3C-$(O{-}CH_2)_2{-}O{-}$) chains, were synthesized by the condensation of two equivalents of 3,5-diiodo-2-hydroxybenzaldehyde with one equivalent of either 4,5-bis(2-methoxyethoxy)benzene-1,2-diamine or 4,5-bis(2-(2-methoxyethoxy)ethoxy) benzene-1,2-diamine under an inert atmosphere and reflux for 1 h (Scheme S1). The species $[Fe^{III}(L^1)Cl]$ (**1**) and $[Fe^{III}(L^2)Cl]$ (**2**) were prepared by the treatment of one equivalent of H_2L^1 or H_2L^2, respectively, with one equivalent of $FeCl_3{\cdot}6H_2O$ salt in methanol under aerobic conditions. This was carried out in the presence of anhydrous $NaOCH_3$ as the base that deprotonates the two phenol groups to form the coordinating phenolates. The FTIR spectroscopic data for species **1** and **2** showed distinct symmetric and asymmetric C−H stretching vibrations at 3055−2817 cm^{-1} regions. Additionally, the C═N stretching vibrations characteristic to the azomethine C═N groups were observed at 1575 and 1578 cm^{-1} for **1** and **2**, respectively. The high-resolution ESI-mass spectrum of **1** and **2** showed *m*/*z* peaks at 1021.7024 and 1145.7282 corresponding to $\{[Fe^{III}(L^1)] - Cl\}^+$ and $\{[Fe^{III}(L^2)Cl] + H^+\}^+$, respectively. The experimental peak isotopic patterns showed good agreement with the simulated spectra. The proposed structural assignments were validated by CHN elemental analysis. Both species show a high-spin $3d^5$ configuration consistent with other previously observed $3d^5$ Fe^{III} metallosurfactants in similar environments[32] and confirmed by DFT calculations.

Electronic Structure and Redox Response. UV−visible spectra of ligands H_2L^1 and H_2L^2 and metallosurfactants $[Fe^{III}(L^1)Cl]$ (**1**), $[Fe^{III}(L^2)Cl]$ (**2**), and $[Fe^{III}(L^{tBu})Cl]$ (**3**) were recorded in 1.0 × 10^{-5} mol·L^{-1} dichloromethane solutions to gain understanding on the electronic structure and the nature of the frontier molecular orbitals engaged with electron transport. The ligands show absorption bands between 285 and 368 nm attributed to $\pi \rightarrow \pi^*$ charge transitions. Both **1** and **2** showed bands in the UV region at 318, 374, and 398 nm and the visible region at 452 nm with molar absorptivity values ranging from 14500 to 33700 L mol^{-1} cm^{-1}, as shown in Figure S1a−b. These absorptions show a bathochromic shift from the values for **3** at 310, 351, and 395, and 452 nm.[6] This shift suggests that the molecular orbitals for **1** and **2** are energetically more accessible than they are for **3**. Based on the previous studies, the absorption bands between 318 to 398 nm can be attributed to ligand-to-metal charge transfer (LMCT) transitions, arguably from the p_π orbitals of phenolate and phenylenediamine moieties to d_{σ^*} and d_{π^*} orbitals of Fe^{III} metal.[33−35] The absorption band at 452 nm was assigned to the intraligand $\pi \rightarrow \pi^*$ charge-transfer (ILCT) transition process from the phenolate's p_π to p_{π^*} of azomethine moiety.[4,6,36−38] Time-dependent DFT (TD-DFT) calculations for **1** and **2**, as shown in Figures S2 and S3, confirmed our proposed charge-transfer transitions. Species **1** shows two bands of $\pi \rightarrow \pi^*$ intraligand charge-transfer transitions (ILCT) at 452 and 437 nm with respective 0.0448 and 0.1076 oscillation strengths. The calculated bands at 318, 381, and 398 nm correspond to the LMCT transitions with oscillation strength values of 0.0935, 0.0721, and 0.0479, respectively. However, species **2** shows only one $\pi \rightarrow \pi^*$ transition at 453 nm with 0.0903 oscillation strength value and three LMCT transitions at 317, 370, and 394 nm with 0.1185, 0.0733, and 0.0427 oscillation strength values, respectively. The experimental and TD-DFT calculated UV−visible spectra for species **2** are shown in Figure 2a-b. We propose that the longer chains in **2** amplify molecular vibrations such as twisting, rocking, wagging, and scissoring, thus momentarily disrupting orbital overlap and lowering the favorability of the $\pi \rightarrow \pi^*$ ILCT process, while not strongly affecting the M−N and M−O bonds and leaving the LMCT transitions mostly unchanged. This is further validated by the observed similarity of the HOMO−LUMO/SOMO energy gaps.

Because d−d transitions are overlapped by intense CT bands, we used DFT calculations to gain insights on the ligand fields and energies of the 3d-based MOs around species **1**−**2**. The results are summarized in Figure 2c. Both metallosurfactants exhibit geometry, in which two Fe−N_{amine} and two Fe−$O_{phenolate}$ bonds form a square base and an axial Fe−Cl completes the coordination environment. The resulting ligand field splitting for **1** and **2** resembles that of a square pyramidal environment, in which the d_{x2-y2} MO is the highest at 35 kcal/mol, followed by the d_{z2} MO separated by a Δvalue of 25 kcal/mol. This gap is smaller than the respective Δ_O values experimentally calculated[39−41] for octahedral $[Fe^{III}(H_2O)_6]^{3+}$ (40 kcal/mol) and $[Fe^{III}(bipyridine)_3]^{3+}$ (57 kcal/mol) and fosters a high-spin environment.

The presence of N_{amine} and $O_{phenolate}$ donors removes the resemblance of an idealized C_{4v} symmetry and leads to the disruption of any expected *e*-like degeneracy with the d_{xz}, d_{xy}, and the lowest lying d_{yz} MOs found, respectively, at ∼9, ∼6, and 0 kcal/mol. In both cases, the lowest lying $3d_{yz}$ is singly occupied in a high-spin configuration, and the most likely to engage in Fe-centered electron transport processes.

Cyclic voltammetry experiments were performed to probe the redox response of **1** and **2**, respectively, in 1.0 × 10^{-3} $molL^{-1}$ dichloromethane and 19:1 dichloromethane: dimethyl sulfoxide solutions using $TBAPF_6$ as the supporting electrolyte. The cyclic voltammograms for **1** and **2** are shown in Figure 3.

https://doi.org/10.1021/acs.jpcc.4c02249
J. Phys. Chem. C XXXX, XXX, XXX−XXX

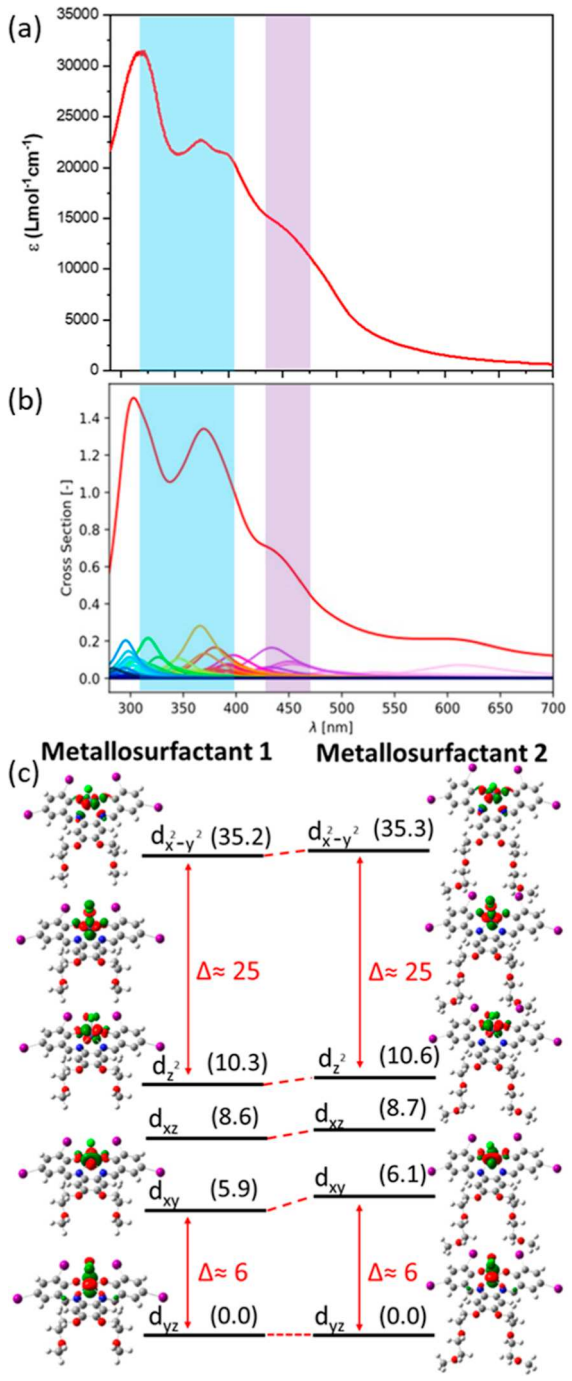

Figure 2. (a) Experimental UV−visible spectrum for **2**; (b) TD-DFT calculated spectrum for **2**. Traces relate to individual calculated excited states with red as the lowest state (S_1), blue as the highest state (S_{150}), and dark red as the resulting spectrum. Peak heights may vary from the experimental spectrum. Bars of blue (ILCT) and purple (LMCT) states are highlighted on both experimental and calculated spectra. (c) DFT calculated ligand field energies of the 3d-based MOs for 1−2. Information for **1** is available in Figure S4.

Species **1** shows a reversible process at −0.08 $V_{Ag/AgCl}$ (−0.63 $V_{Fc/Fc+}$, ΔE_p = 0.16 V, $|I_{pa}/I_{pc}|$ = 1.04) attributed to Fe^{III}/Fe^{II} redox couple and a quasi-reversible process at 1.47 $V_{Ag/AgCl}$ (0.92 $V_{Fc/Fc+}$, ΔE_p = 0.15 V, $|I_{pa}/I_{pc}|$ = 1.23) assigned to phenolate/phenoxyl radical oxidation. Species **2** shows a cathodic reversible Fe^{III}/Fe^{II} redox couple at −0.10 $V_{Ag/AgCl}$ (−0.59 $V_{Fc/Fc+}$, ΔE_p = 0.09 V, $|I_{pa}/I_{pc}|$ = 0.99) and an ill-defined ligand-based oxidation process at 0.78 V (E_{pa}). The tBu-based species **3** showed similar redox properties to **1** and **2**, with an additional second ligand-based oxidation process. In comparison, **3** shows redox processes that are better defined than that in **1** or **2**, but with the redox couple of interest, Fe^{III}/Fe^{II} occurring at the higher reduction potential of −1.02 $V_{Fc/Fc+}$.

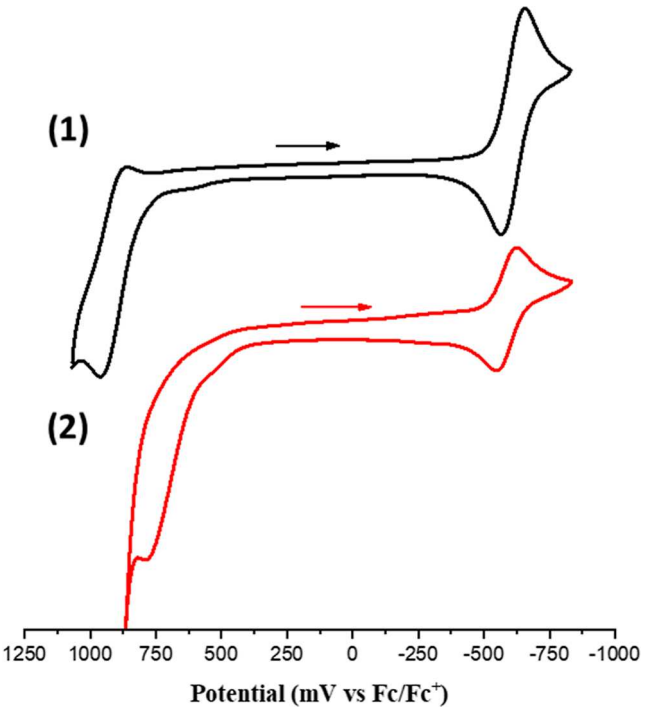

Figure 3. Cyclic voltammograms of metallosurfactants **1** and **2** in dichloromethane and 1:19 DMSO: DCM, respectively. Glassy carbon (WE), Ag/AgCl (RE), Pt wire (CE), and 0.1 M $TBAPF_6$ supporting electrolyte. All potentials recorded vs Fc/Fc^+ couple at a 100 mV/s scan rate.

Air|Water Interfacial Behavior of PL Monolayer Films. The amphiphilic properties of $[Fe^{III}(L^1)Cl]$ (**1**) and $[Fe^{III}(L^2)Cl]$ (**2**) were assessed by surface pressure vs. the average molecular area compression isotherms, by BAM and SEM. The appropriate interfacial behavior of metallosurfactants is necessary to enable the fabrication of Au|LBFilm|Au and Au|LBFilm|EGaIn junctions for electron transport studies. The molecular design for **1** incorporates the polar alkoxy head-groups together with the potential hydrophobic iodo-substituted part that gives this complex the amphiphilic nature. The isotherm for **1** shown in Figure 4a suggests the formation of homogeneous PL[42−45] films at the air/water interface. Species **1** does not show drastic phase transitions and collapses at around 30 mN m^{-1}. This is similar to the observed behavior for metallosurfactant $[Fe^{III}(L^{tBu})Cl]$ (**3**) with collapse at 40 mN m^{-1}. BAM images confirmed the formation of homogeneous PL films between 10 and 28 mN m^{-1} with an average limiting molecular area of approximately 75 $Å^2$. Collapse was characterized by an array of Newton rings,[46] in which matter is ejected due to compression of the multilayers (Figure S6a).

Aiming to improve film formation, we evaluated the effect of subphase polarity using metallosurfactant **1**. Three different subphases were used at a constant temperature and neutral pH for these studies, namely, (i) regular nanopure water, (ii)

https://doi.org/10.1021/acs.jpcc.4c02249
J. Phys. Chem. C XXXX, XXX, XXX−XXX

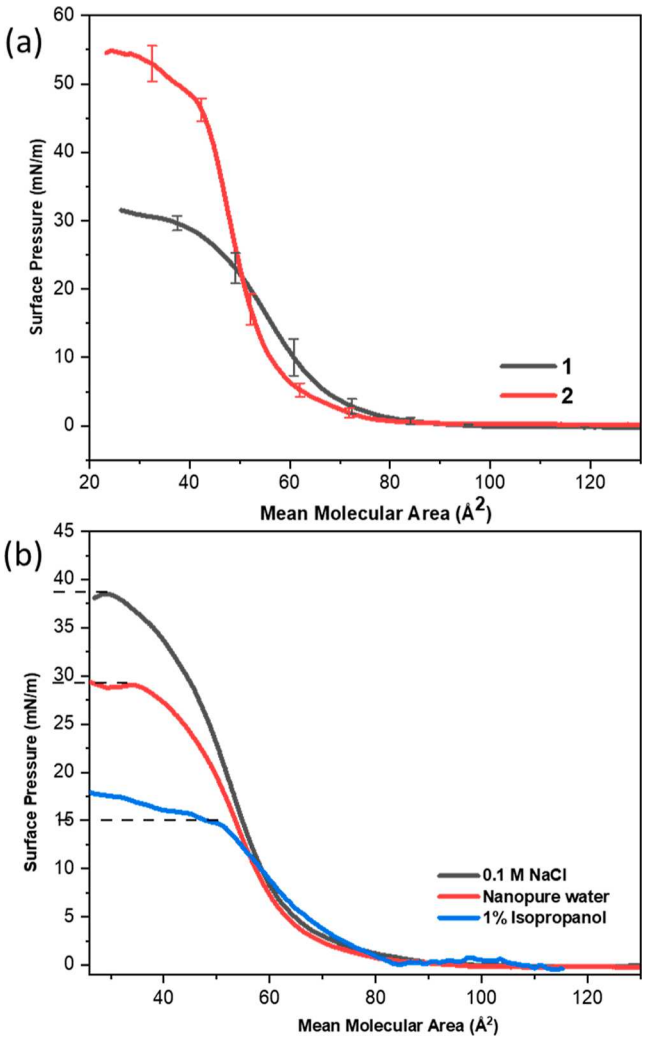

Figure 4. (a) Compression isotherms for **1** and **2**. The vertical error bars show limits over three isothermal compression experiments. (b) Compression isotherms of **1** on nanopure water (red trace), 0.1 M NaCl (black trace), and 1% isopropanol (blue trace) subphases.

hyperpolar media using a 0.1 M NaCl solution and hypopolar media by incorporating 1% isopropanol into water. At least three isothermal compressions were run for each subphase, and the comparative isotherms are shown in Figure 4b. Compared to the nanopure water subphase, with a collapse at ca. 30 mN m^{-1}, the hyperpolar media enhanced PL film formation by improving collapse pressure to ca. 38 mN m^{-1}, whereas hypopolar media decreased the collapse pressure to ca. 15 mN m^{-1}. The comparable average area per molecule suggests that the added NaCl and isopropanol do not interact significantly with the individual metallosurfactants. This is distinct to a related subphase change effect previously studied by our group in which metallosurfactants with {Cu_2} and μ-oxo {Cu_4} cores treated with terephthalate ions showed a likely formation of extended coordination polymers at the air/water interface.[47] As expected, these results confirm that isopropanol is not coordinating and that Na^+ ions from NaCl do not replace the iron ions and inform that species **1** containing iodo substituents exhibits a still prevalent hydrophobic character. As such, we hypothesized that metallosurfactant **2** would exhibit improved amphiphilic behavior due to the extended alkoxy chains. The interfacial behavior of **2** was evaluated from its isothermal compression behavior shown in Figure 4a. Indeed, the compression isotherms for **2** showed enhanced formation of PL films characterized by a collapse pressure improvement to around 50 mN m^{-1}. BAM images (Figure S6b) support homogeneous PL film formation between 10 and 39 mN m^{-1} with an average molecular area of approximately 64 Å^2 indicative of improved packing.

Air|Solid Langmuir−Blodgett Film Deposition and Morphological Analysis. The LB monolayer films of metallosurfactants [$Fe^{III}(L^1)Cl$] (**1**) and [$Fe^{III}(L^2)Cl$] (**2**) were deposited on glass substrates at varying surface pressures and analyzed by SEM. The transfer ratio during isothermal compression was maintained near unity, indicating complete transfer of PL films from air|liquid to LB films onto solid substrates. The SEM analysis, as shown in Figure S7, for **1** shows that the films deposited at the surface pressure of 15 mN m^{-1} yield heterogeneous surface coverage, with an improvement at 20 mN m^{-1} but still displaying characteristic pinhole defects. The films deposited at collapse pressure or above, i.e., 28−35 mN m^{-1} exhibit nonuniform and rough surfaces indicative of molecular aggregates. The monolayer of **1** deposited at 24 mN m^{-1} shows uniform and smooth surface and was considered appropriate for film deposition onto gold-coated mica substrates used for junction fabrication. On the other hand, the SEM images (Figure 5a) for **2** show homogeneous film depositions at surface pressures between 22 and 28 mN m^{-1}.

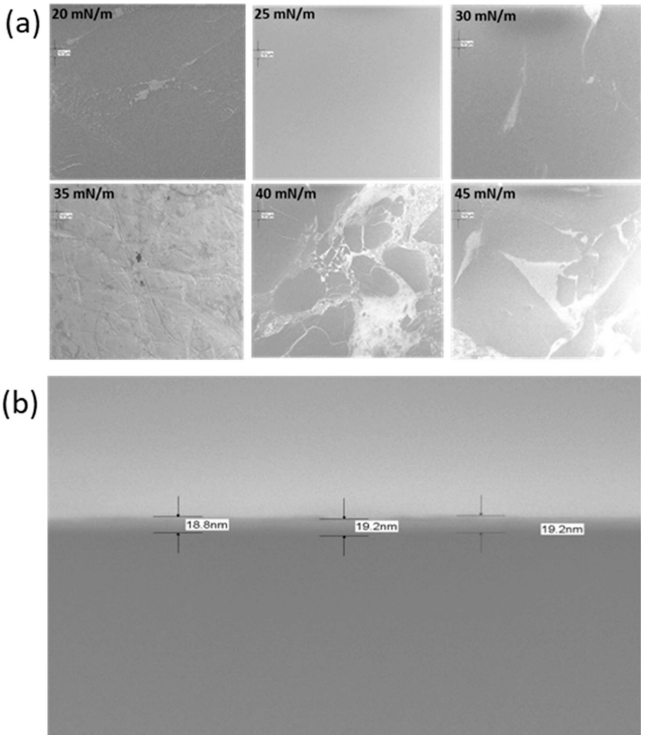

Figure 5. (a) SEM images of monolayers of metallosurfactant **2** deposited on glass substrates at different surface pressures, at 40× magnification under the LM mode. (b) SEM image of cross-section thickness measurements for metallosurfactant **1** (200,000× magnification under the SEM mode). Each film was deposited as 15 monolayers on SiO_2 thermal wafers and measured three times. The mean cross-section thickness was divided by the total number of layers to obtain an approximate monolayer thickness.

https://doi.org/10.1021/acs.jpcc.4c02249
J. Phys. Chem. C XXXX, XXX, XXX−XXX

SEM was further used to determine the monolayer thickness measurements for **1** and **2** using silicon dioxide thermal wafers with 15 and 17 monolayers, respectively. The measurements were carried out in a minimum of five different surface points before the values were averaged. The average thickness for **1** and **2** was established at 12.8 ± 0.25 and 16.3 ± 0.37 Å, respectively (Figures 5b, S8). The molecular lengths for the equivalent molecules were calculated using ab initio molecular dynamics simulations of the optimized structures with the estimated thickness of 12.73 ± 0.34 and 14.50 ± 0.30 Å for **1** and **2**, respectively. The excellent agreement between calculated average length and experimental film thickness is shown in Figure S9 and supports successful deposition of these species.

To assess the structural information on the deposited LB films, the electrospray ionization mass spectrometry (ESI-MS), infrared reflection absorption spectroscopy (IRRAS), UV−visible spectrometry, and XPS methods were used. The obtained information was compared with the data from the bulk complexes. To run IRRAS, UV−visible, and ESI-MS experiments, we used thin films containing ca. 60 monolayers of **1** or **2**, respectively. The LB monolayers were transferred onto glass and gold-coated mica substrates at constant surface pressures of 24 and 25 mN m^{-1}, respectively, by Y-type dipping,[48] deposited in both the up and down directions, at 23 °C. We used *p*-polarized light[49,50] for IRRAS at an angle of incidence of 20° for **1** and 50° for **2** and compared the spectra with the FTIR spectra of the bulk samples, as shown in Figures S10 and S11. The LB films of **1** and **2** and their respective bulk samples showed equivalent peak patterns with symmetric and asymmetric C−H stretching vibrations associated with the alkyl chains of alkoxy groups appearing between 3050 and 2853 and 3050−2819 cm^{-1}, respectively. The slight C−H stretching frequency shifts observed from **1** and **2** can be attributed to good film packing and ordering.[51]

Additionally, both complexes show prominent peaks between 1605 and 1270 cm^{-1} attributed to the C=C, C−O−C, and CH_3/CH_2 deformation bands. A C=N stretching vibration from the film at 1578 and 1583 cm^{-1} for **1** and **2**, respectively, confirm the presence of imine groups, indicating that the ligand structure remains intact after film deposition.[52,53]

The UV−visible characterization of the LB films of metallosurfactants **1** and **2** show excellent spectral agreement with the bulk complexes, as shown in Figure 6. The characteristic LMCT bands are preserved and appear at around 318 to 380 nm for both complexes.

For further identification of the deposited LB films, glass substrates were scraped off the films and analyzed using ESI-MS. The ESI-MS data confirmed the identity between the bulk species **1** with multilayer LB films characterized by the same *m*/*z* values and isotopic distribution, as shown in Figure S13. The LB film monolayers of species **2** show the *m*/*z* value of 1109.7496 for $[Fe^{III}(L^2) - Cl]^+$ as compared to the bulk value of 1145.7282 which corresponds to $[Fe^{III}(L^2)Cl + H^+]^+$ (Figure S14).

XPS experiments were conducted using a thin film containing 10 monolayers of **1** or **2** on gold-coated mica substrates, and their spectral characteristics were compared with the data from microcrystalline bulk species. The general features of the high-resolution spectra for both the bulk and the LB films of **1** and **2** can be discussed together due to their similarity. The results for both samples representing C 1s, Fe 2p, and I 3d spectra are shown in Figures 7 and S15. Both samples display three peaks around 284.8, 286.1, and 288.7 eV for the C 1s spectra, respectively, assigned to the C−C, C−O, and C-δ^+ environments. These environments resemble phenolate ring-containing ligands and electron-deficient carbon atoms.[54] The Fe 2p spectrum recorded for the samples was also analyzed. Four subpeaks at ∼710.0, 711.7, 714.8, and 718.8 eV were required to adequately fit the Fe $2p_{3/2}$ component. The peaks at ∼710.0 and 711.7 eV are associated with Fe^{III}−O environments, while the other two at ∼714.8 and 718.8 eV are satellite peaks. The corresponding Fe $2p_{1/2}$ component shows subpeaks at ∼722.9, 725.2, 728.9, and 732.6 eV associated with Fe^{III}−O environments and satellite peaks.[55−59] Additionally, I 3d spectra recorded for species **1** and **2** were analyzed. The peaks appear, respectively, at ∼620.6 and 632.1 eV assigned to I $3d_{5/2}$ and I $3d_{3/2}$ for C−I environments.[60,61] The elemental information obtained for the bulk and the thin films from high-resolution C 1s, Fe 2p, and I 3d spectra show excellent agreement indicative of structural preservation of metallosurfactants after the film deposition onto the solid substrates.

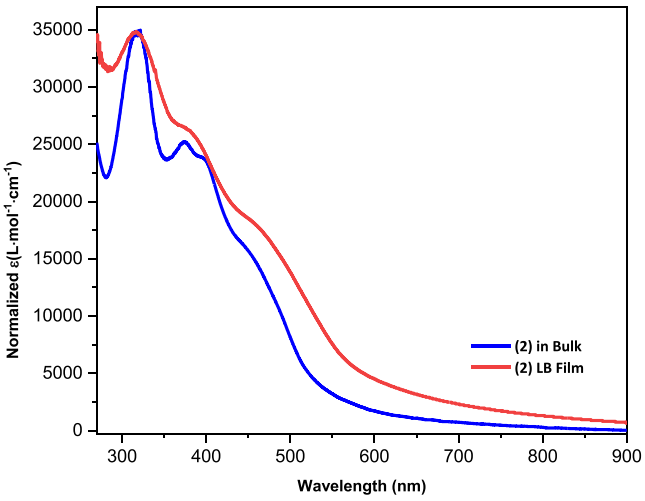

Figure 6. Comparison of UV−visible spectra of **61** layers of LB films for **2** and in solution state UV−visible spectra. Information for metallosurfactant **1** is provided in Figure S12.

Fabrication of Au|LB|Au and Au|LB|EGaIn Junctions. Monolayers of metallosurfactants $[Fe^{III}(L^1)Cl]$ (**1**) or $[Fe^{III}(L^2)Cl]$ (**2**) were, respectively, deposited at 24 and 25 mN m^{-1} on precleaned gold-coated mica substrates. These single monolayers were dried in a desiccator for 5 days under reduced pressure, when a top gold electrode was deposited using the shadow masking method[62] with an Effa-Coater gold sputter yielding Au|LB|Au assemblies. Other Au|LB monolayers were treated with a liquid soft contact electrode of gallium indium eutectic (EGaIn) to yield Au|LB|EGaIn assemblies. The eutectic gallium indium droplet is covered by a disordered adventitious Ga_2O_3 oxide that is reportedly formed due to the contact with air, and therefore the assemblies may be thoroughly described as Au|LB|EGaIn|Ga_2O_3.[63−65] Three Au|LBFilm|Au assemblies for metallosurfactant **1** and four for **2**, each containing 16 junctions were prepared for current−voltage (I−V) analysis at room temperature, totaling 48 and 64 junctions, respectively. A total of 27 Au|LB|EGaIn junctions were prepared for **2**.

https://doi.org/10.1021/acs.jpcc.4c02249
J. Phys. Chem. C XXXX, XXX, XXX−XXX

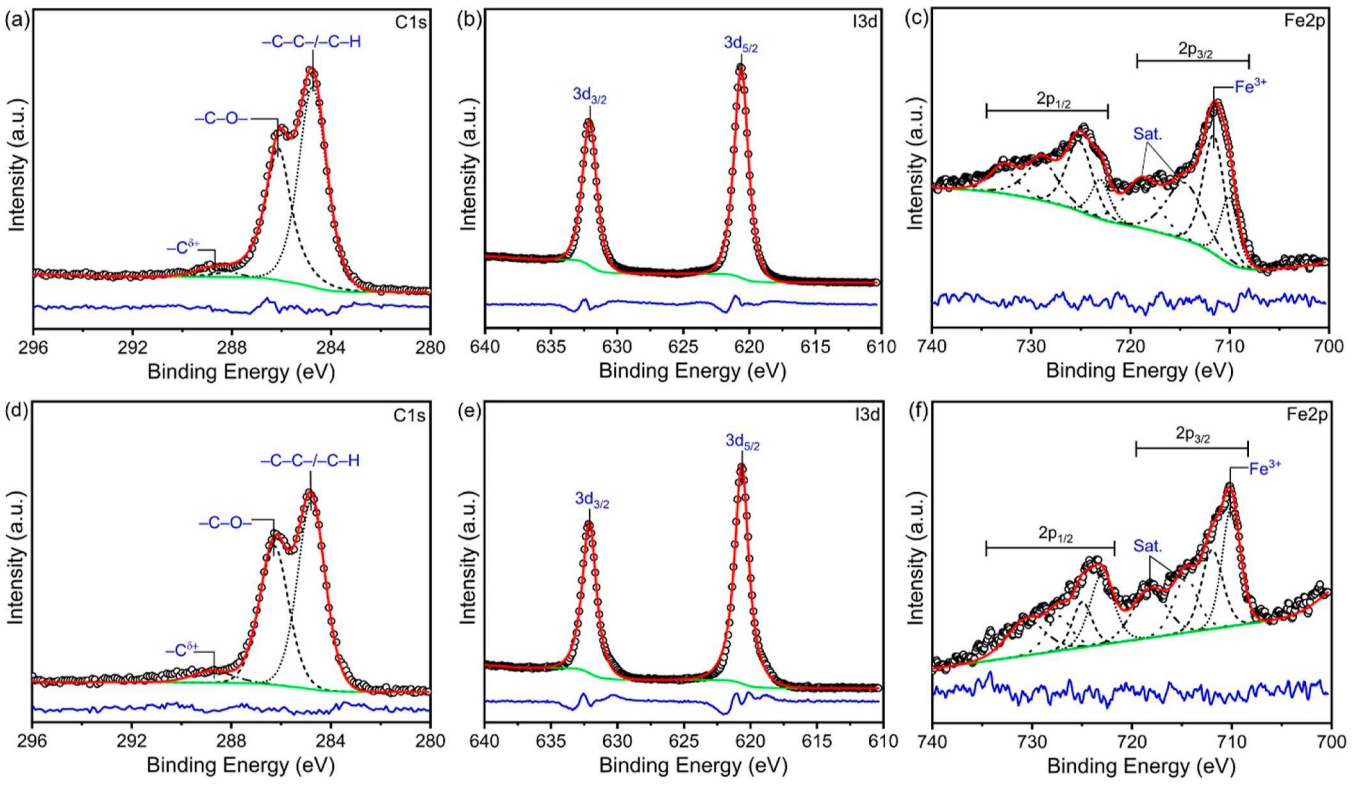

Figure 7. High-resolution XPS C 1s, I 3d, and Fe 2p spectra for **1** as bulk sample (a–c) and as LB monolayers (d–f). The figures show experimental data (circle), calculated fits (red line), background (green line), and residual (blue line–offset for clarity) traces.

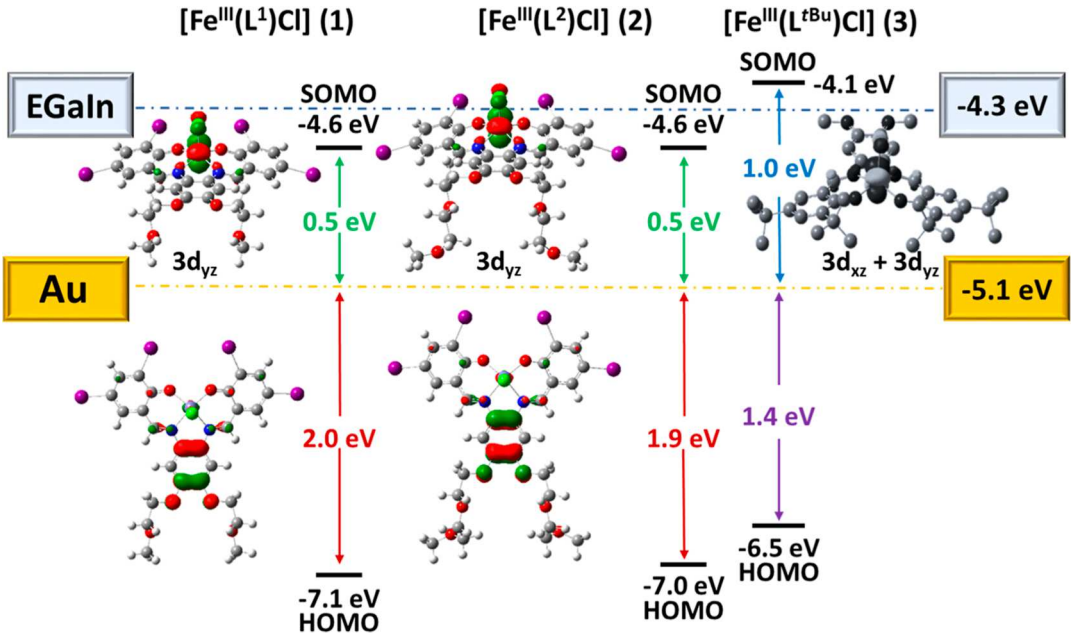

Figure 8. Summary of MO/Fermi energies relevant for electron transport in metallosurfactants **1**, **2**, and **3**.

Feasibility and Observation of Electron Transport. Unidirectional electron transport takes place only if there is energetic compatibility between the Fermi levels (EF) of solid electrodes and the frontier MOs of the metallosurfactant. The experimental determination of the reduction and oxidation electrochemical potentials can be converted from Ag/AgCl into saturated calomel (V_{SCE}) and associated with the energies of the molecular orbitals for metallosurfactants [Fe^{III}(L^1)Cl] (**1**) and [Fe^{III}(L^2)Cl] (**2**). The equivalent solid-state energies associated with the first electron affinity (V_a) and the first ionization (V_i) energies can, then, be calculated by the Hipps and Armstrong approximation[66−68] considering V_a = 4.7 eV + $E_{1/2}^{red}$ (SCE), and V_i = 4.7 eV + 1.7$E_{1/2}^{ox}$ (SCE), and conveniently compared to the Fermi energy of the electrodes.

Estimated values for Au Fermi levels vary.[2,69−72] The value of 5.1 eV is commonly accepted for Au(111), reaching up to 5.30 eV. Similar values are reported to polycrystalline Au, whereas Au(100) and Au(110) are usually listed at ∼5.20 eV.

https://doi.org/10.1021/acs.jpcc.4c02249
J. Phys. Chem. C XXXX, XXX, XXX−XXX

We adopt the value of 5.10 eV (or −5.10 eV below the vacuum level) because film deposition and molecular self-assembly studies tend to report the 111 surface.[73−75] The liquid metal EGaIn electrode shows Fermi levels at −4.30 eV.[11,12,52,76−78]

The first metal-based singly occupied MO for **1** showed an estimated V_a value of −4.58 eV, thus 0.52 eV above the gold electrode Fermi levels. On the other hand, the energy of the ligand-based highest-occupied MO is −7.12 eV, which is 2.02 eV below the Fermi levels of the gold electrode. Metallosurfactant **2** showed comparable energies with V_a = −4.56 eV (0.54 eV above Au Fermi levels) and V_i = −6.95 eV (1.85 eV below Fermi). When EGaIn is considered, the metal-based SOMO for **1** or **2** sits ∼0.3 eV below that electrode's Fermi level. This distribution of energies is depicted in Figure 8.

We measured experimentally the electron transport behavior for **1** or **2** in several Au|LB|Au and Au|LB|EGaIn junctions by means of current−voltage (I−V) measurements in order to assess the differences between (i) substituents in **1** and [$Fe^{III}(L^{tBu})Cl$] (**3**), (ii) chain length and film assembly in **1** and **2**, and (iii) electrodes in junctions Au|LB**2**|Au and Au|LB**2**|EGaIn, expecting that each of these comparisons lead to noticeable changes in current and rectification ratios. Metallosurfactants **1** and **2** were, respectively, tested in three and four Au|LB|Au assemblies. Due to monolayer defects, several junctions were short circuited. Species **1** had a failure rate of ∼46% (22 junctions), whereas **2** showed significantly lower failure rate of ∼27%. A total of 23 junctions (∼89%) for species **1** and 39 junctions (∼83%) for species **2** yielded asymmetric curves in which current response was elevated in the negative quadrant and negligible in the positive quadrant, as indicative of rectifying or unidirectional electron transport behavior. A total of 2 assemblies with 27 Au|LB|EGaIn junctions were analyzed for species **2**. From these junctions, 21 of them (∼78%) yielded asymmetric curves, whereas the remaining 22% were short circuited. Figure 9a−c summarizes the data.

Comparison of iodo-substituted species **1** and *t*-Bu substituted species **3** probed as Au|LB**1**|Au showed that metallosurfactant **1** had verified rectification behavior at applied biases of ±2, ±3, and ±4 V. The ±2 V curve offers good comparison with **3**; species **1** displays an observed current of −1.7 nA, while a value of −0.8 nA was reported by **3**.[5] The observed rectification ratio, given by the product between negative and positive currents or RR = [I at − V/I at + V], in species **1** varied from 2 to 10 at a biased voltage range of ±2 V and from 4 to 15 at ±4 V. For species **3**, it varied from 4 to 28 between ±2 V and from 2 to 31 between ±4 V. The higher current is attributed to the significant lowering of the SOMO-Fermi energy occasioned by the presence of iodo substituents, whereas the slightly lower RR values are tentatively associated with a less favorable packing of the monolayer, that may predispose some metallosurfactant detachment.[62]

The effect of chain length on film assembly and electron transport for both iodo-substituted species **1** and **2** probed as Au|LB**1**|Au and Au|LB**2**|Au showed the described results for **1** along with a current of −1.0 nA at ±2 V and RR variation from 6 to 14 between ±2 V and 8 to 30 between ±4 V for **2**. This observation confirms our hypothesis that extending the alkoxy chain would lead to improved amphiphilic balance and enhance film formation and transfer onto the solid substrate, ultimately leading to comparable electron transport between **2** and **3**. The observed lower currents for **2** are tentatively attributed to an increased tunneling distance.[50,79−83] A similar behavior was reported for cobaltocene-based species.[12,84] The

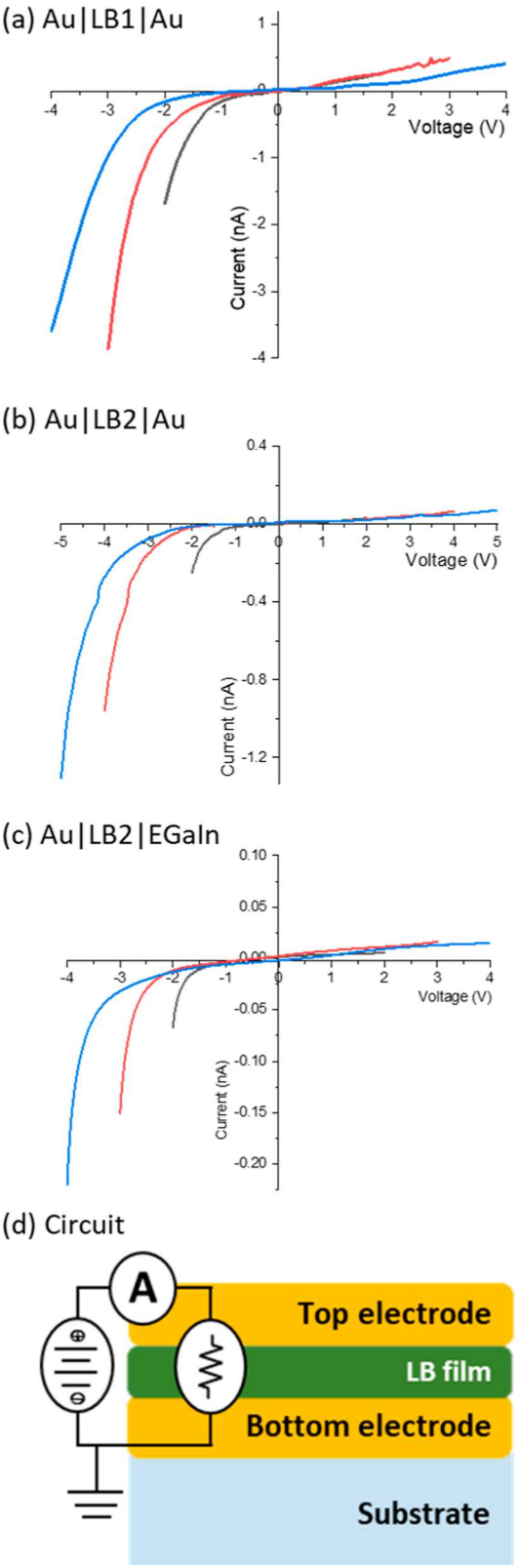

Figure 9. Asymmetric I−V curves for (a) **1** in Au|LB**1**|Au between ±2, ±3, and ±4 V; (b) **2** in Au|LB**2**|Au between ±2, ±4, and ±5 V; (c) **2** in Au|LB**2**|EGaIn between ±2, ±3, and ±4 V; and (d) circuit diagram for E1|LB|E2. Other I−V curves for Au|LB**1**|Au, Au|LB**2**|Au, and Au|LB**2**|EGaIn are available in Figures S16, S17, and S18.

https://doi.org/10.1021/acs.jpcc.4c02249
J. Phys. Chem. C XXXX, XXX, XXX−XXX

match between the Fermi and SOMO energy levels in metallosurfactants **1** and **2** indicates better feasibility of unidirectional electron transport than that of *t*-Bu-substituted **3**.

Comparison of electrodes was carried out by probing the current−voltage response of iodo-substituted species **2**. Each assembly had a bias voltage applied to the top electrode, Au in Au|LB**2**|Au or EGaIn in Au|LB**2**|EGaIn, while maintaining the bottom gold electrode at zero bias voltage. The intrinsic difficulty in the latter case is the assessment of appropriate Fermi level energy, considering the asymmetry between $E_{F(Au)}$ = −5.10 and $E_{F\ (EGaIn)}$ = −4.30 eV. Species **2** should have a better EGaIn Fermi-MO energy match of ca. 0.3 eV compared to Au Fermi-MO at ca. 0.5 eV. Asymmetric I−V curves at selected ±4 V applied bias confirmed unidirectional electron transfer with $RR_{Au|Au}$ = 8 to 30, whereas $RR_{Au|EGaIn}$ ranged between 8 and 18. Although somewhat decreased, these comparable results suggest that electron transfer occurs through similar mechanisms and molecular orbitals.

Experimental Confirmation of MO Used in Electron Transport. Estimations provided by cyclic voltammetry to MO energies were obtained by conversion of the reduction potentials into solid-state energies.[85] However, the $^{HS}3d^5$ ion Fe^{III} displays unpaired electrons in its electronic configuration and reduction entails population of the lowest singly occupied SOMO. On the other hand, the oxidation process is centered on the phenolate or phenylenediamine moiety of the ligand[3,25,86−88] and therefore associated with an available highest occupied HOMO. Considering the Fermi energy level of pristine Au at −5.1 eV under vacuum, both species $[Fe^{III}(L^1)Cl]$ (**1**) and $[Fe^{III}(L^2)Cl]$ (**2**) show a gap of 0.5 eV between the lowest lying metal-based SOMO and electrode Fermi, while the ligand-based HOMO-Fermi gap is, respectively, estimated at 2.0 and 1.9 eV. To measure experimentally the energies of the relevant molecular orbitals, we used UPS on films of **1** and **2**, each containing 11 monolayers deposited on Au-coated mica substrates. The UPS spectra observed for LB films of **1** and **2** are shown in Figures 10a−c and S19. The experimental work functions are shown at 4.0 and 4.1 eV for **1** and **2**, respectively. The Δvalues of SOMO/HOMO levels of the $3d^5$ Fe^{III} species of **1** and **2** were measured at 1.5 and 1.4 eV, respectively. These measurements show good agreement with the ligand-based HOMO energies of **1** and **2** and a good trend agreement with the calculated Δvalues from cyclic voltammetry. Further validation comes from DFT calculations, which allow us to compare the calculated orbital energies with solid-state conversion of the electrochemical potentials and the energies obtained from UPS. The calculated HOMO-SOMO energy gap from DFT compares well at 2.1 eV for species **1** and 2.0 eV for **2**. The lowest SOMO in both complexes represents the $3d_{yz}$ orbital with predominant metal character with 3d orbital splitting patterns shown in Figure S5.

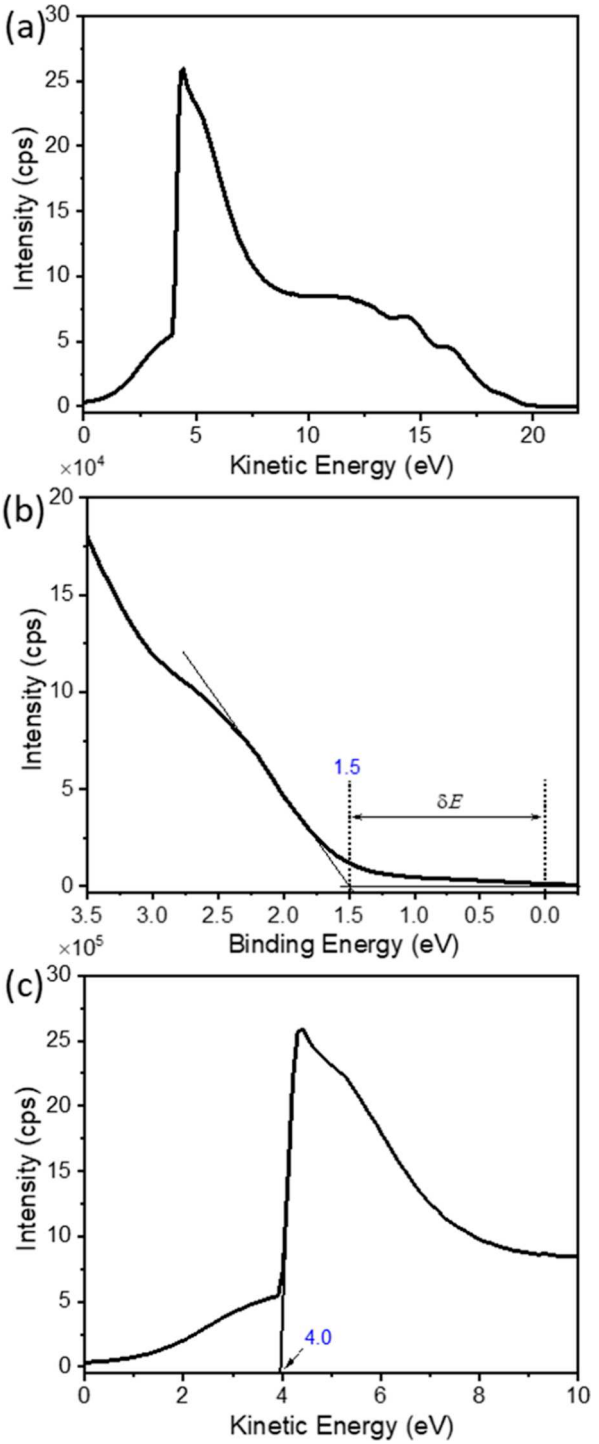

Figure 10. UPS (He I) spectrum for metallosurfactant **1** deposited on the Au substrate. (a) Full UPS spectrum; (b) lower binding energy region of the UPS spectrum; and (c) zoomed-in view of the secondary electron cutoff.

CONCLUSIONS

This study evaluated the influence of peripheral molecular changes on the energies of SOMO and HOMO orbitals respective to the Fermi levels of Au and EGaIn electrodes. We developed two new metallosurfactants, $[Fe^{III}(L^1)Cl]$ (**1**) and $[Fe^{III}(L^2)Cl]$ (**2**), in which iodo-substituents replace well-established *t*-butyl groups in N_2O_2 environments, and longer methoxy-diethoxy chains replace the established methoxye-thoxy chains. We studied the electronic, electrochemical, and interfacial behavior of these species varying subphase polarity before we scrutinized their ability to promote directional electron transport as monolayer films on Au|LB|Au and Au|LB|EGaIn junctions. The results were compared to our *t*-Bu-substituted standard $[Fe^{III}(L^{tBu})Cl]$ (**3**). In order to address a single variable at a time, discussion of MO energies is most meaningful between species **1** and **3** containing distinct substituents, while discussion of film properties includes

https://doi.org/10.1021/acs.jpcc.4c02249
J. Phys. Chem. C XXXX, XXX, XXX−XXX

species **1** and **2** with distinct chain lengths. The most distinguished feature came with the introduction of electron-withdrawing iodo substituents that led to a decrease in the value of the reduction potential attributed to the Fe^{III}/Fe^{II} redox couple of **1** and **2**, both at −0.6 $V_{Fc/Fc+}$ Comparing this potential in **1** to that of **3 at**, this at −1.0 $V_{Fc/Fc+}$. On the other hand, the iodo-substituted species displayed a less reversible phenolate/phenoxyl first oxidation process. The presence of iodo groups led to some amphiphilic imbalance characterized by a somewhat low collapse pressure of 30 mN m^{-1} observed in **1**. This imbalance could be addressed using hyperpolar media, or the installation of longer alkoxy chains in **2**, which then displayed a collapse near 50 mN m^{-1}. Once monolayer films were deposited and studied, it became clear that the introduction of electron-withdrawing substituents favored significant modulation of the Au Fermi-SOMO energy gap, reflected by a lowering of the conducting $3d_{xz}$ +$3d_{yz}$ degenerate MOs at about 1.0 eV above Fermi in **3** to about relative position of the conducting $3d_{yz}$ in **1** and **2** at 0.5 eV above Fermi.

Use of distinct electrodes Au (−5.10 eV) or EGaIn (−4.30 eV) with pronounced energy asymmetry in the same junction led to limited understanding of the transport pathways. Nonetheless, the comparable results between Au|LB|Au and Au|LB|EGaIn are suggestive of similar mechanisms and molecular orbitals.

The use of EGaIn electrodes, together with selection of electronic configuration, and installation of electron-withdrawing substituents will provide relevant levers to understand and control unidirectional electron transport by molecular monolayers.

■ ASSOCIATED CONTENT

Supporting Information

The Supporting Information is available free of charge at https://pubs.acs.org/doi/10.1021/acs.jpcc.4c02249.

Details on ligand synthesis; UV−visible spectra for bulk and films and TD-DFT results; SEM morphology and thickness of films; XPS measurements; I−V curves; and XYZ coordinates of DFT calculated structures (PDF)

■ AUTHOR INFORMATION

Corresponding Author

Cláudio N. Verani − *Department of Chemistry, Wayne State University, Detroit, Michigan 48202, United States;* orcid.org/0000-0001-6482-1738; Email: claudio.verani@wayne.edu

Authors

Gibson Kirui − *Department of Chemistry, Wayne State University, Detroit, Michigan 48202, United States*

Widana Kaushalya − *Department of Chemistry, Wayne State University, Detroit, Michigan 48202, United States*

S. Sameera Perera − *Lumigen Instrument Center, Department of Chemistry, Wayne State University, Detroit, Michigan 48202, United States*

Alice R. Walker − *Department of Chemistry, Wayne State University, Detroit, Michigan 48202, United States;* orcid.org/0000-0002-8617-3425

Complete contact information is available at: https://pubs.acs.org/10.1021/acs.jpcc.4c02249

Author Contributions

G.K. contributed to the investigation, formal analysis, and methodology for synthesis, characterization, electrochemistry, PL and Langmuir−Blodgett film studies, SEM, assembly and junction fabrication and analysis, data management, and writing of the original draft. W.K. contributed to the formal calculations, analysis, and writing of the original draft for DFT calculations. S.S.P. contributed to the formal analysis and methodology for X-ray and UV photoelectron spectroscopy. A.R.W. contributed to the formal analysis, supervision, advising to W.K., and writing of DFT section. C.N.V. provided the overall conceptualization, data curation, formal analysis, funding acquisition, project administration, supervision, and writing (review and editing) of the manuscript.

Notes

The authors declare no competing financial interest.

■ ACKNOWLEDGMENTS

The authors thankfully acknowledge support from the National Science Foundation −NSF through the grants NSF-CHE1904584 and NSF-CHE1012413 to C.N.V., including financial support to G.K. Support from the Wayne State University for startup funds and through grant NSF-CHE2338804 to A.R.W., including financial support to W.K. are also acknowledged. This work made use of the UPS/XPS facility that was partially funded through grant NSF-MRI-1849578. We also acknowledge the WSU-Lumigen Instrument Center high-resolution mass spectrometry resources supported by grant R01 GM098285-07S1 from the National Institutes of Health, and we thank the WSU Supercomputing Grid for computational support.

■ REFERENCES

(1) Jensen, P. W. K.; Kristensen, L. B.; Lavigne, C.; Aspuru-Guzik, A. Toward Quantum Computing with Molecular Electronics. *J. Chem. Theory Comput.* **2022**, *18*, 3318−3326.

(2) Ollitrault, P. J.; Miessen, A.; Tavernelli, I. Molecular Quantum Dynamics: A Quantum Computing Perspective. *Acc. Chem. Res.* **2021**, *54*, 4229−4238.

(3) Bayliss, S. L.; Laorenza, D. W.; Mintun, P. J.; Kovos, B. D.; Freedman, D. E.; Awschalom, D. D. Optically addressable molecular spins for quantum information processing. *Science* **2020**, *370*, 1309−1312.

(4) Gaita-Ariño, A.; Luis, F.; Hill, S.; Coronado, E. Molecular spins for quantum computation. *Nat. Chem.* **2019**, *11*, 301−309.

(5) Atzori, M.; Sessoli, R. The Second Quantum Revolution: Role and Challenges of Molecular Chemistry. *J. Am. Chem. Soc.* **2019**, *141*, 11339−11352.

(6) Metzger, R. M. Unimolecular Electronics. *Chem. Rev.* **2015**, *115*, 5056−5115.

(7) Xiang, D.; Wang, X.; Jia, C.; Lee, T.; Guo, X. Molecular-Scale Electronics: From Concept to Function. *Chem. Rev.* **2016**, *116*, 4318−4440.

(8) Lanznaster, M.; Hratchian, H.; Heeg, M. J.; Hryhorczuk, L.; McGarvey, B.; Schlegel, H. B.; Verani, C. N. Structural and Electronic Behavior of Unprecedented Five-Coordinate Iron(III) and Gallium-(III) Complexes with a New Phenol-Rich Electroactive Ligand. *Inorg. Chem.* **2006**, *45*, 955−957.

(9) Wickramasinghe, L.; Perera, M.; Li, L.; Mao, G.-Z.; Zhou, Z.-X.; Verani, C. N. Rectification in Nanoscale Devices Based on an Asymmetric Five-Coordinate Iron(III) Phenolate Complex. *Angew. Chem., Int. Ed.* **2013**, *52*, 13346−13350.

(10) Wickramasinghe, L.; Mazumder, S.; Gonawala, S.; Perera, M. M.; Baydoun, H.; Thapa, B.; Li, L.; Xie, L.; Mao, G.; Zhou, Z.; et al. The Mechanisms of Rectification in Au|Molecule|Au Devices Based

on Langmuir−Blodgett Monolayers of Iron(III) and Copper(II) Surfactants. *Angew. Chem., Int. Ed.* **2014**, *53*, 14462−14467.
(11) Wickramasinghe, L. D.; Mazumder, S.; Kpogo, K. K.; Staples, R. J.; Schlegel, H. B.; Verani, C. N. Electronic Modulation of the SOMO−HOMO Energy Gap in Iron(III) Complexes towards Unimolecular Current Rectification. *Chem.—Eur. J.* **2016**, *22*, 10786−10790.
(12) Liu, R.; Ke, S.-H.; Yang, W.; Baranger, H. U. Organometallic molecular rectification. *J. Chem. Phys.* **2006**, *124*, 024718.
(13) Nijhuis, C. A.; Reus, W. F.; Whitesides, G. M. Mechanism of Rectification in Tunneling Junctions Based on Molecules with Asymmetric Potential Drops. *J. Am. Chem. Soc.* **2010**, *132*, 18386−18401.
(14) Kornilovitch, P.; Bratkovsky, A.; Stanley Williams, R. Current rectification by molecules with asymmetric tunneling barriers. *Phys. Rev. B* **2002**, *66*, 165436.
(15) Ellenbogen, J. C.; Love, J. C. Architectures for molecular electronic computers. I. Logic structures and an adder designed from molecular electronic diodes. *Proc. IEEE* **2000**, *88*, 386−426.
(16) Weeraratne, A. D. K. I.; Rani, N.; Amunugama, S.; Perera, S. S.; Kpogo, K. K.; Mazumder, S.; Verani, C. N. Influence of Electronic Configurations on the Modulation of Fermi/Orbital Junction Energies for Directional Electron Transport through 3d1, 3d3, and 3d5Metallosurfactants. *J. Phys. Chem. C* **2022**, *126*, 21010−21021.
(17) Cousino, A.; Wickramasinghe, L. D.; Kaushalya, W.; Perera, S. S.; Baydoun, H.; Walker, A.; Verani, C. N. Studies on Monolayer Formation and Electron Transport in Au|LB|Au Junctions Containing 3d4MnIII Metallosurfactants. *J. Phys. Chem. C* **2023**, *127*, 16654−16667.
(18) Johnson, M. S.; Horton, C. L.; Gonawala, S.; Verani, C. N.; Metzger, R. M. Observation of current rectification by a new asymmetric iron(III) surfactant in a eutectic GaIn|LB monolayer|Au sandwich. *Dalton Trans.* **2018**, *47*, 6344−6350.
(19) Johnson, M.; Wickramasinghe, L.; Verani, C. N.; Metzger, R. M. Confirmation of the Rectifying Behavior in a Pentacoordinate [N2O2] Iron(III) Surfactant Using a "Eutectic GaIn|LB Monolayer| Au" Assembly. *J. Phys. Chem. C* **2016**, *120*, 10578−10583.
(20) Weeraratne, A. D. K. I.; Baydoun, H.; Shakya, R.; Niklas, J.; Xie, L.; Mao, G. Z.; Stoian, S.; Poluektov, O.; Verani, C. N. Observation of current rectification by the new bimetallic iron(III) hydrophobe [FeIII2(LN4O6)] on Au|LB-molecule|Au devices. *Dalton Trans.* **2018**, *47*, 14352−14361.
(21) Parr, R. G. Density functional theory of atoms and molecules. In *Horizons of Quantum Chemistry: Proceedings of the Third International Congress of Quantum Chemistry*; Springer, 1980, pp 5−15.
(22) Frisch, M. J.; Trucks, G. W.; Schlegel, H. B.; Scuseria, G. E.; Robb, M. A.; Cheeseman, J. R.; Scalmani, G.; Barone, V.; Mennucci, B.; Petersson, G. A.; et al. *Gaussian 16*, Revision. B.01; Gaussian, Inc.: Wallingford, CT, 2016.
(23) Vosko, S. H.; Wilk, L.; Nusair, M. Accurate spin-dependent electron liquid correlation energies for local spin density calculations: a critical analysis. *Can. J. Phys.* **1980**, *58*, 1200−1211.
(24) Lee, C.; Yang, W.; Parr, R. G. Development of the Colle-Salvetti correlation-energy formula into a functional of the electron density. *Phys. Rev. B* **1988**, *37*, 785−789.
(25) Francl, M. M.; Pietro, W. J.; Hehre, W. J.; Binkley, J. S.; Gordon, M. S.; DeFrees, D. J.; Pople, J. A. Self-consistent molecular orbital methods. XXIII. A polarization-type basis set for second-row elements. *J. Chem. Phys.* **1982**, *77*, 3654−3665.
(26) Hariharan, P. C.; Pople, J. A. The influence of polarization functions on molecular orbital hydrogenation energies. *Theor. Chim. Acta* **1973**, *28*, 213−222.
(27) Scalmani, G.; Frisch, M. J. Continuous surface charge polarizable continuum models of solvation. I. General formalism. *J. Chem. Phys.* **2010**, *132*, 114110.
(28) Liu, F.; Luehr, N.; Kulik, H. J.; Martinez, T. J. Quantum Chemistry for Solvated Molecules on Graphical Processing Units Using Polarizable Continuum Models. *J. Chem. Theory Comput.* **2015**, *11*, 3131−3144.
(29) Dennington, R.; Keith, T.; Millam, J. *GaussView*, version 5(8); Semichem Inc.: Shawnee Mission, KS, 2009.
(30) Ufimtsev, I. S.; Martinez, T. J. Quantum Chemistry on Graphical Processing Units. 3. Analytical Energy Gradients, Geometry Optimization, and First Principles Molecular Dynamics. *J. Chem. Theory Comput.* **2009**, *5*, 2619−2628.
(31) Isborn, C. M.; Luehr, N.; Ufimtsev, I. S.; Martínez, T. J. Excited-State Electronic Structure with Configuration Interaction Singles and Tamm−Dancoff Time-Dependent Density Functional Theory on Graphical Processing Units. *J. Chem. Theory Comput.* **2011**, *7*, 1814−1823.
(32) Imbert, C.; Hratchian, H. P.; Lanznaster, M.; Heeg, M. J.; Hryhorczuk, L. M.; McGarvey, B. R.; Schlegel, H. B.; Verani, C. N. Influence of ligand rigidity and ring substitution on the structural and electronic behavior of trivalent iron and gallium complexes with asymmetric tridentate ligands. *Inorg. Chem.* **2005**, *44*, 7414−7422.
(33) Gaber, B. P.; Miskowski, V.; Spiro, T. G. Resonance Raman scattering from iron(III)- and copper(II)-transferrin and an iron(III) model compound. Spectroscopic interpretation of the transferrin binding site. *J. Am. Chem. Soc.* **1974**, *96*, 6868−6873.
(34) Mayilmurugan, R.; Suresh, E.; Palaniandavar, M. A New Tripodal Iron(III) Monophenolate Complex: Effects of Ligand Basicity, Steric Hindrance, and Solvent on Regioselective Extradiol Cleavage. *Inorg. Chem.* **2007**, *46*, 6038−6049.
(35) Velusamy, M.; Palaniandavar, M.; Gopalan, R. S.; Kulkarni, G. U. Novel Iron(III) Complexes of Tripodal and Linear Tetradentate Bis(phenolate) Ligands: Close Relevance to Intradiol-Cleaving Catechol Dioxygenases. *Inorg. Chem.* **2003**, *42*, 8283−8293.
(36) Rotthaus, O.; Jarjayes, O.; Philouze, C.; Del Valle, C. P.; Thomas, F. One-electron oxidized nickel(II) complexes of bis and tetra(salicylidene) phenylenediamineSchiff bases: from monoradical to interacting Ni(III) ions. *Dalton Trans.* **2009**, *14* (10), 1792−1800.
(37) Shongwe, M. S.; Kaschula, C. H.; Adsetts, M. S.; Ainscough, E. W.; Brodie, A. M.; Morris, M. J. A Phenolate-Induced Trans Influence: Crystallographic Evidence for Unusual Asymmetric Coordination of an α-Diimine in Ternary Complexes of Iron(III) Possessing Biologically Relevant Hetero-Donor N-Centered Tripodal Ligands. *Inorg. Chem.* **2005**, *44*, 3070−3079.
(38) Auerbach, U.; Eckert, U.; Wieghardt, K.; Nuber, B.; Weiss, J. Synthesis and coordination chemistry of the hexadentate ligands 1,4,7-tris(2-hydroxybenzyl)-1,4,7-triazacyclononane (H3L1) and 1,4,7-tris(3-tert-butyl-2-hydroxybenzyl)-1,4,7-triazacyclononane (H3L2). Crystal structures of $[HL^{1}Cu^{II}]$ and $[L^{2}Fe^{III}]$acacH. *Inorg. Chem.* **1990**, *29*, 938−944.
(39) Figgis, B. N.; Hitchman, M. A. *Ligand Field Theory and its Applications*; Wiley VCH, 2000; pp 218−219.
(40) Huheey, J. E. *Inorganic Chemistry: Principles of Structure and Reactivity*, Harper-Collins, 1983, 3rd ed, pp 385−386.
(41) Dunn, T. M.; McClure, D. S.; Pearson, R. G. *Some aspects of Crystal Field Theory Table 4.1*; Harper & Row: New York, 1965; p 82.
(42) The inclusion of the name Pockels to the films commonly referred to as Langmuir monolayers aims to address a historical omission toward the pioneering work of citizen scientist Agnes Pockels (1862−1935) in the understanding of film formation at the air−water interface. See Rayleigh, L.; Pockels, A. Surface tension. *Nature* **1891**, *43*, 437−439.
(43) Pockels, A. On the relative contamination of the water-surface by equal quantities of different substances. *Nature* **1892**, *46*, 418−419.
(44) Pockels, A. Relations between the surface-tension and relative contamination of water surfaces. *Nature* **1893**, *48*, 152−154.
(45) Pockels, A. On the spreading of oil upon water. *Nature* **1894**, *50*, 223−224.
(46) Castillo-Chará, J.; Lucchese, R. R.; Bevan, J. W. Differentiation of the ground vibrational and global minimum structures in the Ar: HBr intermolecular complex. *J. Phys. Chem. C* **2001**, *115*, 899−911.
(47) Hindo, S. S.; Shakya, R.; Shanmugam, R.; Heeg, M. J.; Verani, C. N. Metalloamphiphiles with [Cu2] and [Cu4] headgroups:

https://doi.org/10.1021/acs.jpcc.4c02249
J. Phys. Chem. C XXXX, XXX, XXX−XXX

syntheses, structures, langmuir films, and effect of subphase changes. *Eur. J. Inorg. Chem.* **2009**, *2009*, 4686−4694.
(48) Petty, M. C. *Langmuir Blodgett Films: An Introduction*; Cambridge University Press: New York, 1996.
(49) Brezesinski, G.; Dobner, B.; Stefaniu, C.; Vollhardt, D. Monolayer Characteristics of an N-Acylated Ethanolamine at the Air/Water Interface. *J. Phys. Chem. C* **2011**, *115*, 8206−8213.
(50) Wang, L.; Cruz, A.; Flach, C. R.; Pérez-Gil, J.; Mendelsohn, R. Langmuir-Blodgett films formed by continuously varying surface pressure. Characterization by IR spectroscopy and epifluorescence microscopy. *Langmuir* **2007**, *23*, 4950−4958.
(51) Hamoudi, H.; Chesneau, F.; Patze, C.; Zharnikov, M. Chain length-dependent branching of irradiation-induced processes in alkanethiolate self-assembled monolayers. *J. Phys. Chem. C* **2011**, *115*, 534−541.
(52) Nakamoto, K. *Infrared and Raman Spectra of Inorganic and Coordination Compounds, Part B: Applications in Coordination, Organometallic and Bioinorganic Chemistry*, 6th ed.; Wiley: Hoboken, 2008, pp 1−222.
(53) Lipert, R. J.; Lamp, B. D.; Porter, M. D. *Modern Techniques in Applied Molecular Spectroscopy*; Mirabella, F. M., Ed.; Wiley: New York, 1998; pp 83−126.
(54) Yamamoto, Y.; Toyota, E. Paramagnetic cobalt (III) complexes with organic ligands. IX. the preparation and properties of paramagnetic tetraammine (5-nitrosalicylideneaminato) cobalt (III) complexes. *Bull. Chem. Soc. Jpn.* **1986**, *59*, 617−620.
(55) Biesinger, M. C.; Payne, B. P.; Grosvenor, A. P.; Lau, L.; Gerson, A. R.; Smart, R. Resolving surface chemical states in XPS analysis of first row transition metals, oxides and hydroxides: Cr, Mn, Fe, Co and Ni. *Appl. Surf. Sci.* **2011**, *257*, 2717−2730.
(56) Skrzypek, D.; Szymanska, B.; Kovala-Demertzi, D.; Wiecek, J.; Talik, E.; Demertzis, M. A. Synthesis and spectroscopic studies of iron (III) complex with a quinolone family member (pipemidic acid). *J. Phys. Chem. Solids* **2006**, *67*, 2550−2558.
(57) Conradie, J.; Erasmus, E. XPS Fe 2p peaks from iron tris(β-diketonates): Electronic effect of the β-diketonato ligand. *Polyhedron* **2016**, *119*, 142−150.
(58) Mullet, M.; Khare, V.; Ruby, C. XPS study of Fe(II)−Fe(III) (oxy)hydroxycarbonate green rust compounds. *Surf. Interface Anal.* **2008**, *40*, 323−328.
(59) Yamashita, T.; Hayes, P. Analysis of XPS spectra of Fe2+ and Fe3+ ions in oxide Materials. *Appl. Surf. Sci.* **2008**, *254*, 2441−2449.
(60) Zhou, X.-L.; Solymosi, F.; Blass, P. M.; Cannon, K. C.; White, J. M. Interactions of methyl halides (Cl, Br, and I) with Ag(111). *Surf. Sci.* **1989**, *219*, 294−316.
(61) Zhou, X.-L.; White, J. M. Alkyl halide photochemistry on Ag(111): III. Methyl iodide. *Surf. Sci.* **1991**, *241*, 270−278.
(62) Metzger, R. M.; Chen, B.; Höpfner, U.; Lakshmikantham, M. V.; Vuillaume, D.; Kawai, T.; Wu, X.; Tachibana, H.; Hughes, T. V.; Sakurai, H.; et al. Unimolecular Electrical Rectification in Hexadecylquinolinium Tricyanoquinodimethanide. *J. Am. Chem. Soc.* **1997**, *119*, 10455−10466.
(63) Johnson, M. S.; Kota, R.; Mattern, D. L.; Hill, C. M.; Vasiliu, M.; Dixon, D. A.; Metzger, R. M. A two-faced "Janus-like" unimolecular rectifier exhibits rectification reversal. *J. Mater. Chem. C* **2014**, *2*, 9892−9902.
(64) Chiechi, R. C.; Weiss, E. A.; Dickey, M. D.; Whitesides, G. W. Eutectic Gallium−Indium (EGaIn): A Moldable Liquid Metal for Electrical Characterization of Self-Assembled Monolayers. *Angew. Chem., Int. Ed.* **2008**, *47*, 142−144.
(65) Reus, W. F.; Thuo, M. M.; Shapiro, N. D.; Nijhuis, C. A.; Whitesides, G. M. The SAM, Not the Electrodes, Dominates Charge Transport in Metal-Monolayer//Ga2O3/Gallium-Indium Eutectic Junctions. *ACS Nano* **2012**, *6*, 4806−4822.
(66) Price, B. K.; Tour, J. M. Functionalization of single-walled carbon nanotubes "on water. *J. Am. Chem. Soc.* **2006**, *128*, 12899−12904.
(67) Scudiero, L.; Barlow, D. E.; Hipps, K. W. Scanning tunneling microscopy, orbital-mediated tunneling spectroscopy, and ultraviolet photoelectron spectroscopy of nickel (II) octaethylporphyrin deposited from vapor. *J. Phys. Chem. B* **2002**, *106*, 996−1003.
(68) Valiyaveettil, S.; Müllen, K. Multiphase self-assembly of 5-alkoxyisophthalic acid and its applications. *New J. Chem.* **1998**, *22*, 89−95.
(69) de la Llave, E.; Clarenc, R.; Schiffrin, D. J.; Williams, F. J. Organization of alkane amines on a gold surface: Structure, surface dipole, and electron transfer. *J. Phys. Chem. C* **2014**, *118*, 468−475.
(70) Skriver, H. L.; Rosengaard, N. M. Surface energy and work function of elemental metals. *Phys. Rev. B* **1992**, *46*, 7157−7168.
(71) Hansson, G. V.; Flodstrom, S. A. Photoemission study of the bulk and surface electronic structure of single crystals of gold. *Phys. Rev. B* **1978**, *18*, 1572−1585.
(72) Michaelson, H. B. The work function of the elements and its periodicity. *J. Appl. Phys.* **1977**, *48*, 4729−4733.
(73) Lee, J. M.; Park, E. J.; Cho, S. H.; Chang, S. Cu-facilitated C− O bond formation using N-hydroxyphthalimide: efficient and selective functionalization of benzyl and allylic C− H bonds. *J. Am. Chem. Soc.* **2008**, *130*, 7824−7825.
(74) Brand, I.; Juhaniewicz-Debinska, J.; Wickramasinghe, L.; Verani, C. N. An in situ spectroelectrochemical study on the orientation changes of an [Fe III L N2O3] metallosurfactant deposited as LB films on gold electrode surfaces. *Dalton Trans.* **2018**, *47*, 14218−14226.
(75) Kitagawa, K.; Morita, T.; Kimura, S. Electron transfer in metal− molecule− metal Junction composed of self-assembled monolayers of helical peptides carrying redox-active ferrocene units. *Langmuir* **2005**, *21*, 10624−10631.
(76) Chelvayohan, M.; Mee, C. H. B. Work Function Measurements on (110), (100) and (111) Surfaces of Silver. *J. Phys. C: Solid State Phys.* **1982**, *15*, 2305−2312.
(77) Giesen, K.; Hage, F.; Himpsel, F. J.; Riess, H. J.; Steinmann, W.; Smith, N. V. Effective Mass of Image-Potential States. *Phys. Rev. B* **1987**, *35*, 975−978.
(78) Monreal, R. C.; Guillemot, L.; Esaulov, V. A. On Auger Neutralization of He^+ Ions on a Ag(111) Surface. *J. Phys.: Condens. Matter* **2003**, *15*, 1165−1171.
(79) Frath, D.; Nguyen, V. Q.; Lafolet, F.; Martin, P.; Lacroix, J.-C. Electrografted monolayer based on a naphthalene diimide-ruthenium terpyridine complex dyad: efficient creation of large-area molecular junctions with high current densities. *Chem. Commun.* **2017**, *53*, 10997−11000.
(80) Souto, M.; Yuan, L.; Morales, D. C.; Jiang, L.; Ratera, I.; Nijhuis, C. A.; Veciana, J. Tuning the Rectification Ratio by Changing the Electronic Nature (Open-Shell and Closed-Shell) in Donor− Acceptor Self-Assembled Monolayers. *J. Am. Chem. Soc.* **2017**, *139*, 4262−4265.
(81) Yuan, L.; Breuer, R.; Jiang, L.; Schmittel, M.; Nijhuis, C. A. A Molecular Diode with a Statistically Robust Rectification Ratio of Three Orders of Magnitude. *Nano Lett.* **2015**, *15*, 5506−5512.
(82) Amunugama, S.; Asempa, E.; Tripathi, R. C.; Wanniarachchi, D.; Baydoun, H.; Hoffmann, P.; Jakubikova, E.; Verani, C. N. Electron transport through a (terpyridine) ruthenium metallo-surfactant containing a redox-active aminocatechol derivative. *Dalton Trans.* **2022**, *51*, 8425−8436.
(83) Larade, B.; Bratkovsky, A. M. Current rectification by simple molecular quantum dots: An ab initio study. *Phys. Rev. B* **2003**, *68*, 235305.
(84) Park, J.; Pasupathy, A. N.; Goldsmith, J. I.; Chang, C.; Yaish, Y.; Petta, J. R.; Rinkoski, M.; Sethna, J. P.; Abruña, H. D.; McEuen, P. L.; et al. Coulomb blockade and the Kondo effect in single-atom transistors. *Nature* **2002**, *417*, 722−725.
(85) Jaggi, N.; Vij, D. R. *Handbook of Applied Solid State Spectroscopy*; Springer: New York, NY, 2006, pp 411−450.
(86) Lanznaster, M.; Heeg, M. J.; Yee, G. T.; McGarvey, B. R.; Verani, C. N. Design of Molecular Scaffolds Based on Unusual Geometries for Magnetic Modulation of Spin-Diverse Complexes with Selective Redox Response. *Inorg. Chem.* **2007**, *46*, 72−78.

https://doi.org/10.1021/acs.jpcc.4c02249
J. Phys. Chem. C XXXX, XXX, XXX−XXX

(87) Allard, M. M.; Sonk, J. A.; Heeg, M. J.; McGarvey, B. R.; Schlegel, H. B.; Verani, C. N. Bioinspired Five-Coordinate Iron(III) Complexes for Stabilization of Phenoxyl Radicals. *Angew. Chem., Int. Ed.* **2012**, *51*, 3178−3182.
(88) Shakya, R.; Allard, M. M.; Johann, M.; Heeg, M. J.; Rentschler, E.; Shearer, J. M.; McGarvey, B.; Verani, C. N. Modeling the Geometric, Electronic, and Redox Properties of Iron(III)-Containing Amphiphiles with Asymmetric [NN′O] Headgroups. *Inorg. Chem.* **2011**, *50*, 8356−8366.

https://doi.org/10.1021/acs.jpcc.4c02249
J. Phys. Chem. C XXXX, XXX, XXX−XXX